DOI: 10.1002/chem.201001636

Crystal Facet Dependence of Water Oxidation on $BiVO_4$ Sheets under Visible Light Irradiation

Donge Wang,[a, b] Hongfu Jiang,[a] Xu Zong,[a] Qian Xu,[a, b] Yi Ma,[a, b] Guoling Li,[a] and Can Li*[a]

Abstract: Monoclinic $BiVO_4$ crystals with preferentially exposed (040) facets were hydrothermally synthesized by using a trace amount of $TiCl_3$ as the directing agent; this function was confirmed by X-ray diffraction patterns (XRD) and high-resolution transmission electron microscopy (HRTEM). The effects of the directing agent $TiCl_3$ and the pH values applied during synthesis have been studied, and the optimized $BiVO_4$ sample with highly exposed (040) facet could be obtained by using 1.2 at.% of $TiCl_3$ as the directing agent at a pH value of 2. Some complementary techniques were also applied to exclude the effects of the structural and physical property changes, such as surface area and hydrophilicity. The photocatalytic activity of oxygen evolution on $BiVO_4$ is found to be proportionally correlated with the exposed surfaces of the (040) facet. It is assumed that the active sites with a BiV_4 structure on the exposed (040) facet is assigned to be responsible for the high activity of O_2 evolution.

Keywords: $BiVO_4$ · crystal engineering · crystal growth · oxygen · photocatalysis

Introduction

Photocatalytic splitting of water into H_2 and O_2 has attracted much attention, because it is an ideal way to produce hydrogen utilizing solar energy.[1–3] Water splitting involves redox processes that include two half reactions: 1) a water reduction reaction ($2H^+ + 2e^- \rightarrow H_2$, i.e., proton reduction) and 2) a water oxidation reaction ($2H_2O \rightarrow 4H^+ + O_2 + 4e^-$). The water oxidation reaction is more challenging for overall water splitting,[4] because it is a four-electron transfer and energetically uphill reaction. To achieve high efficiency of overall water splitting, better understanding of water oxidation reaction and the development of water oxidation photocatalysts is needed. Up to now, many photocatalysts have been reported, but only very few of them are active for overall water splitting under visible light, and the efficiencies are still quite low.[5] Therefore, further investigations into the photocatalytic O_2 evolution is of great importance for achieving overall water splitting with high efficiency.

The catalytic activity of a semiconductor-based photocatalyst can be influenced by its surface structure that is directly exposed to the reaction media. Over the past decades, surface chemists have made great efforts in the study of chemical properties of defined crystal planes.[6,7] Very recently, Lu and co-workers reported that micron-sized anatase TiO_2 crystallites with highly energetic exposed (001) facets can dramatically enhance the photocatalytic activity of H_2 production from water splitting.[8,9] Moreover, sheet-like anatase and micro-sheet anatase TiO_2 showed excellent photocatalytic activity for the degradation of methyl orange and 4-chlorophenol, respectively, due to the exposure of a high percentage of (001) facets.[10,11] It was reported that unique ZnO nanodisks with particular facet showed better photocatalytic activity for photodecomposition of methylene blue and Rhodamine B.[12,13] $BiVO_4$ nanosheets, synthesized in the presence of sodium dodecyl benzene sulfonate, showed a preferred (010) surface orientation and demonstrated good visible-light photocatalytic activities for degradation of Rhodamine B.[14] Lately, Ye et al. reported that $BiVO_4$ nanoplates with exposed (010) facets (corresponding to the (040) peak in the XRD patterns) prepared in aqueous ethanolamine solution showed enhanced photocatalytic activity.[15]

[a] D. Wang, H. Jiang, X. Zong, Q. Xu, Y. Ma, Dr. G. Li, Prof. Dr. C. Li
State Key Laboratory of Catalysis
Dalian Institute of Chemical Physics
Chinese Academy of Sciences
457 Zhongshan Road, Dalian, 116023 (P.R. China)
Fax: (+86) 411-846-94447
E-mail: canli@dicp.ac.cn

[b] D. Wang, Q. Xu, Y. Ma
Graduate School of the Chinese Academy of Sciences (P.R. China)

Supporting information for this article is available on the WWW under http://dx.doi.org/10.1002/chem.201001636.

All of these results indicate that the photocatalytic activity could be directly correlated with the crystal facets of the photocatalyst.

$BiVO_4$ has been reported to be a visible-light-active photocatalyst for the water oxidation reaction[16–19] and the two-step overall water splitting, the so-called Z-scheme type system.[20–22] In this work, the $BiVO_4$ photocatalysts with different growth extent of the (040) facet were hydrothermally synthesized by using a trace amount of $TiCl_3$ as the directing agent in inorganic solution under hydrothermal synthesis conditions. We found that the photocatalytic water oxidation could be considerably enhanced with the growth of the (040) facet of $BiVO_4$, and that the photocatalytic O_2 evolution is dependent on the growth extent of the (040) facet.

Results and Discussion

Role of $TiCl_3$ directing agent in the growth of the (040) facet of $BiVO_4$: The XRD patterns of the $BiVO_4$ samples synthesized with different amounts of directing agents are given in Figure 1a. It can be seen that the $BiVO_4$-**a**, synthesized without using the directing agent, is in the form of monoclinic scheelite (standard card of No. 14-0688, space group: $I2/a$, $a=5.195$, $b=11.701$, $c=5.092$, $\beta=90.38°$) with characteristic diffraction peaks at 15.1, 18.6, 18.9, 28.6, 28.8, 28.9, and 30.5°. These diffraction peaks were also observed for samples $BiVO_4$-**b**, **c**, **d**, **e**, and **f**, indicating that the monoclinic scheelite structures of $BiVO_4$ were well preserved in these samples. However, expanded XRD patterns of $BiVO_4$ samples (Figure 1b) in the range of 28–31° show remarkable variations of the three strong characteristic peaks at ($\bar{1}21$), (121), and (040) for the $BiVO_4$ samples synthesized by the addition of the $TiCl_3$ directing agent.

The dominant diffraction peak for $BiVO_4$-**a** sample is the ($\bar{1}21$) peak at about 28.8°, while the (040) diffraction peaks at about 30.5° become stronger for the $BiVO_4$-**b**, **c**, **d**, **e**, and **f** samples synthesized with the directing agent $TiCl_3$. The intensity of the (040) diffraction peak reaches the maximum for the $BiVO_4$-**d** sample when the Ti/Bi ratio is 1.2 at.%. The domination of the (040) diffraction peak clearly implies that the addition of directing agent facilitates the growth of the $BiVO_4$ crystals toward the (040) facet instead of the ($\bar{1}21$) facet. It should be noted that the intensity of the (020) diffraction peak at 15.1° also increased significantly upon the addition of the directing agent.

The normalization of the XRD intensity for comparison was performed using the (110) peak as the internal standard. Figure 1c shows the correlations of the intensity ratios of (040)/(110) and ($\bar{1}21$)/(110) for the $BiVO_4$ samples synthesized with different amounts of directing agent. It can be seen from Figure 1c that there is no apparent dependence of the ($\bar{1}21$)/(110) intensity ratio on the amount of directing agent added. However, the $BiVO_4$-**a** synthesized without addition of $TiCl_3$ has quite low (040)/(110) intensity ratio. Increasing the amount of the directing agent from 0 to 2.0% (Ti/Bi molar ratio) resulted in the increase of the (040)/(110) intensity ratio from 1.1 at Ti/Bi=0 to the maximum 11.2 at Ti/Bi=1.2%, and then decreases to 5.7 at Ti/Bi=2.0%. These XRD results indicate that $TiCl_3$ directing agent can direct the orientation of the $BiVO_4$ crystal growth preferentially along the (040) facet.

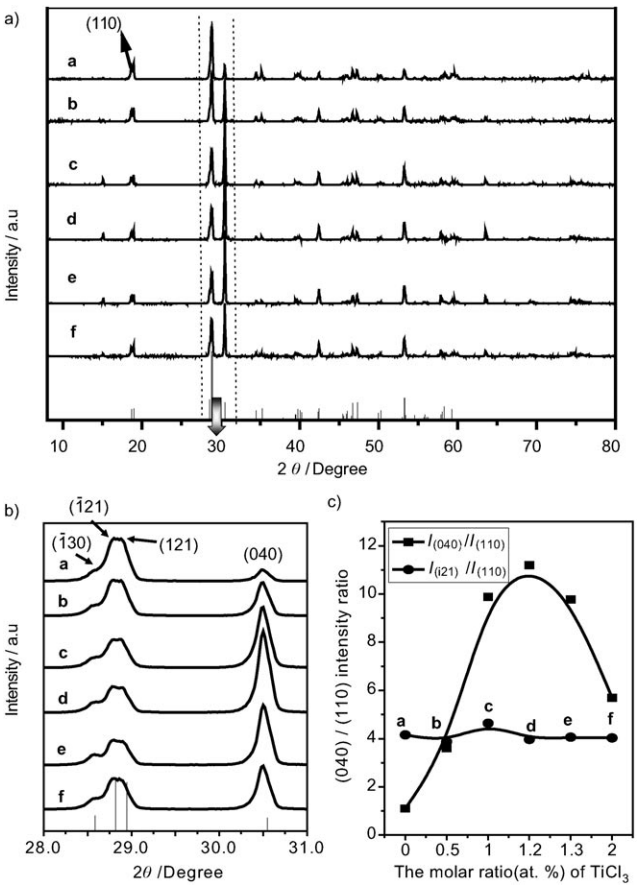

Figure 1. XRD patterns of the $BiVO_4$ samples synthesized with different concentrations of directing agent $BiVO_4$-**a**–**f** (see the Supporting Information for more details). a) XRD patterns of $BiVO_4$ were recorded in the range of 8 to 800. b) Expanded XRD patterns showing the hyperfine structures of the ($\bar{1}21$) and (040) diffraction peaks. c) The correlations of the Ti/Bi molar ratio with the intensity ratios of (040)/(110) and ($\bar{1}21$)/(110) in the XRD patterns of the corresponding BiVO4 samples, and the intensity was normalized using the (110) diffraction peak as an internal standard.

To clarify the role of $TiCl_3$, some other Ti-containing precursors were also used as the directing agent for the synthesis of $BiVO_4$ under the same experimental conditions. XRD patterns (Figure 2a) of the $BiVO_4$ samples synthesized with different Ti-containing precursors as directing agents, other than $TiCl_3$, show no evident enhancement of the (040) peak. Compared with $TiCl_3$, we can know that the anion in the Ti-containing precursor is crucial for the enhancement of (040) peak. Besides, to further confirm the role of $TiCl_3$, various metal chlorides were also tested as Cl-containing precursors. XRD patterns shows that most of them have no particular effects on the enhancement of the (040) peak (Figure 2b), so it is important to use right metal chlorides as the directing agent for the enhancement of (040) peak. In a word,

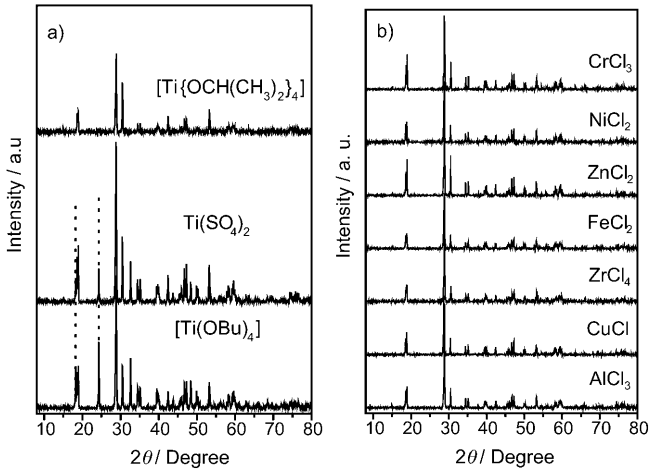

Figure 2. XRD patterns of a) the $BiVO_4$ samples synthesized with different Ti-containing precursors as the directing agent and b) the $BiVO_4$ samples synthesized with different chlorides as the directing agent. The characteristic peaks of the tetragonal $BiVO_4$ are indicated by a dotted line when $Ti(OBu)_4$ and $Ti(SO_4)_2$ were used as Ti-containing precursors.

$TiCl_3$ is found to be a most efficient directing agent for the synthesis of $BiVO_4$ with the greatly enhanced (040) peak intensity.

pH effects on the growth of the (040) facet of $BiVO_4$: Figure 3 also shows the XRD patterns of $BiVO_4$ samples prepared at various pH values. From Figure 3a, we can see that all the XRD patterns of $BiVO_4$ samples are well preserved for the monoclinic phase. The strongest peaks in the XRD patterns (Figure 3b) are 30.5° (040) peak for the $BiVO_4$ samples prepared at pH 2, which are different from 28.8° ($\bar{1}21$) peak for $BiVO_4$; meanwhile, the peak at 15.1° also increases. As the pH value increased, the intensities of peaks (040) for $BiVO_4$ samples decrease distinctly. For $BiVO_4$-**d**, **g**, and **h** prepared at pH <7, the relative intensities of the (040) diffraction peak are stronger than that of $BiVO_4$ prepared without using the directing agent. For the $BiVO_4$-**i**, **j**, **k**, and **l** samples obtained at pH value ≥ 7, the intensities of the (040) diffraction peak are much weaker than that of $BiVO_4$ prepared without using the directing agent, and the ($\bar{1}21$) diffraction peak becomes the dominant peak. Figure 3c shows the dependence of the XRD peak intensity ratio between (040)/(110) and ($\bar{1}21$)/(110) on the pH value. Evidently, the ratio of the intensity between (040) peak and the normalized ($\bar{1}21$) peak decreases greatly with the increase of the pH value. As the pH value increases from 2 to 11, the XRD patterns show that the (040)/(110) intensity ratio decreases sharply from 11.2 for $BiVO_4$-**d** to 0.6 for $BiVO_4$-**l** (Figure 3c). However, the ($\bar{1}21$)/(110) intensity ratio hardly changes with the increase of the pH value. The results indicate that higher pH value during the hydrothermal process has a detrimental effect on the formation of (040) crystal plane. The results of the exposed (040) facets obtained in various hydrothermal pH value systems are also controllable, similar to that of various concentrations of

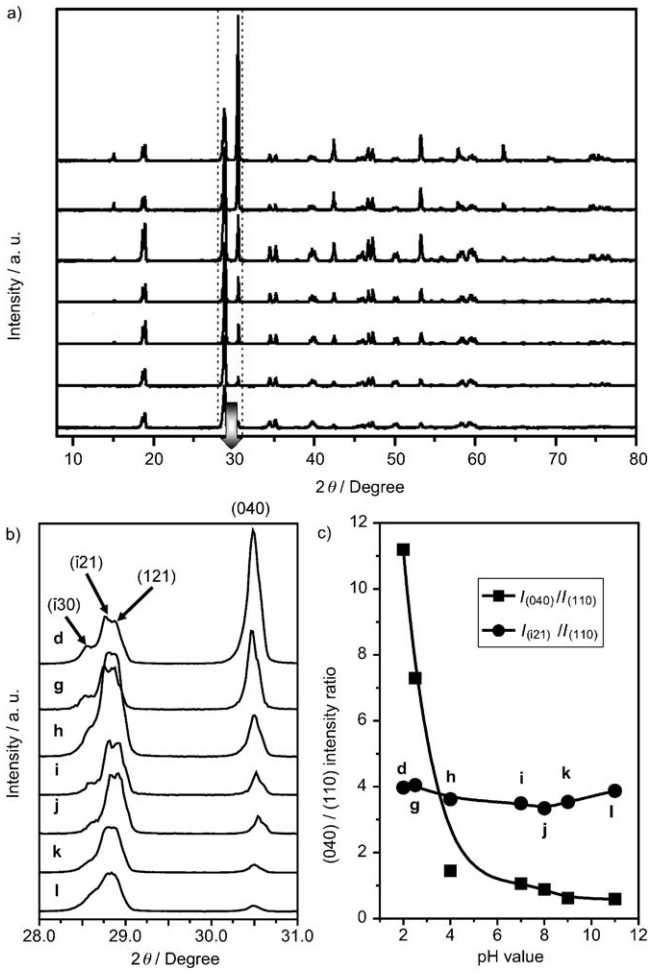

Figure 3. XRD patterns of the $BiVO_4$ samples synthesized with the optimum amount of directing agent under different pH values: **d**: pH 2, **g**: pH 2.5, **h**: pH 4, **i**: pH 7, **j**: pH 8, **k**: pH 9, and **l**: pH 11. a) XRD patterns of $BiVO_4$ were recorded in the range of 8 to 800. b) Expanded XRD patterns showing the hyperfine structures of the ($\bar{1}21$) and (040) diffraction peaks. c) The correlations of the pH value with the intensity ratios of (040)/(110) and ($\bar{1}21$)/(110) in the XRD patterns of the corresponding $BiVO_4$ samples, and the intensity was normalized with the (110) diffraction peak as an internal standard.

$TiCl_3$ directing agent. Therefore, we can synthesize $BiVO_4$ with enhanced intensity of (040) diffraction peak using the directing agent $TiCl_3$ followed by adjusting the pH value. Namely, $BiVO_4$ with more exposed (040) facet can be synthesized by optimizing the concentration of the directing agent and pH value.

Morphologies of $BiVO_4$ samples: $BiVO_4$ has various morphologies that could be controlled by the synthesis methods and experimental conditions.[18,23,24] To visualize the morphology of $BiVO_4$ samples, SEM was used to investigate the $BiVO_4$ samples synthesized under different experimental conditions. Large compact particles (about 2 μm in size) of decagonal shape were observed for $BiVO_4$-**a** synthesized without the addition of the directing agent (Figure 4a). There is a negligible quantity of small irregular particles ad-

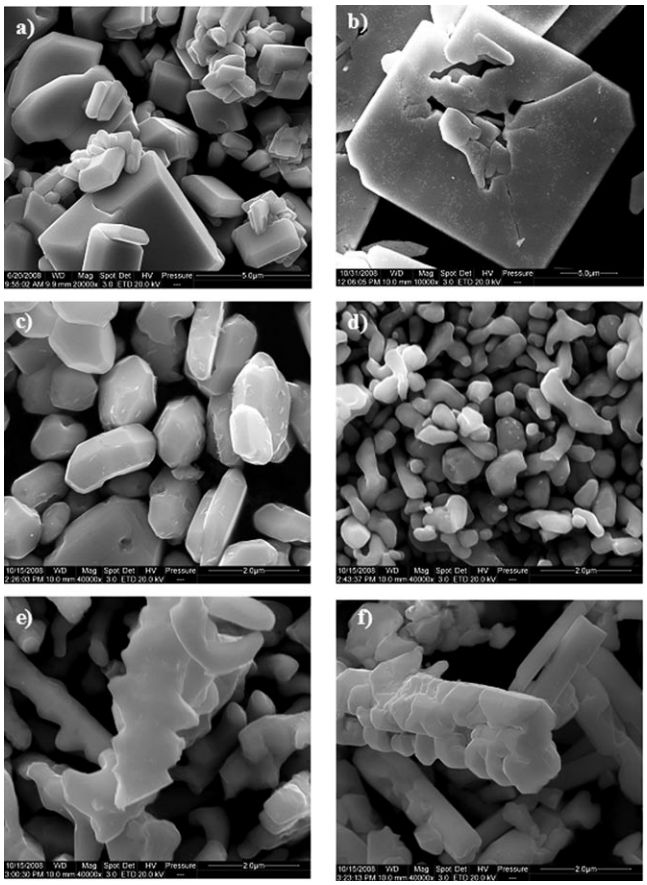

Figure 4. SEM images of a) $BiVO_4$-**a**, b) $BiVO_4$-**d**, c) $BiVO_4$-**h**, d) $BiVO_4$-**i**, e) $BiVO_4$-**k**, and f) $BiVO_4$-**l**.

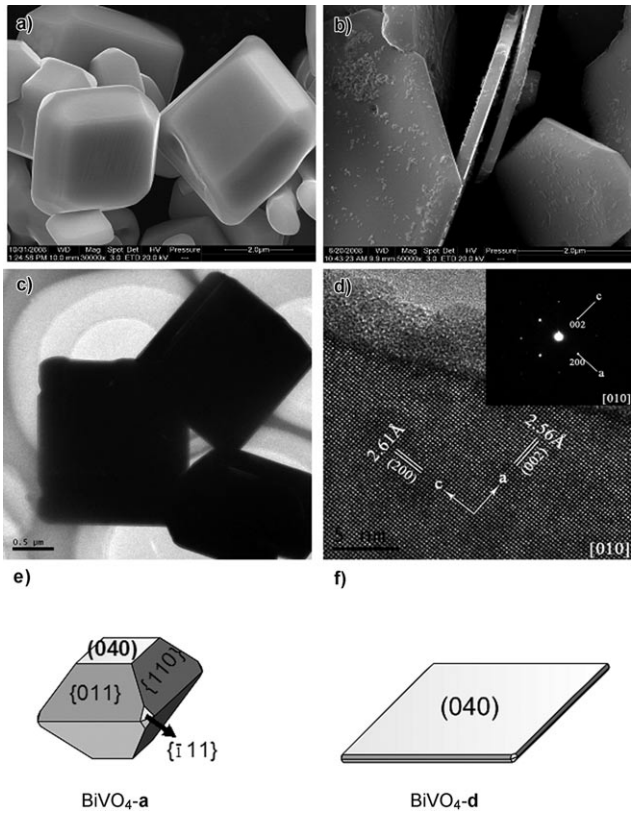

Figure 5. SEM images of samples of a) $BiVO_4$-**a** and b) $BiVO_4$-**d**. HRTEM images of samples of c) $BiVO_4$-**a** and d) $BiVO_4$-**d** with its SEAD pattern. Schematic illustrations for e) BiVO4-**a** and f) $BiVO_4$-**d**. Note, [*uvw*] is an index of a specified crystal axis and (*hkl*) is an index of a specified crystal plane, while {*hkl*} indicates a set of the group crystal planes with the same atomic configuration.

hering to the decagonal particles. The particles show smooth surface and are highly crystallized with decagonal shape. These particles have with well-defined, relatively sharp edges. The morphology of $BiVO_4$-**d**, with the most intense (040) peak, is distinct from that of $BiVO_4$-**a**. The SEM images of $BiVO_4$-**d** showed sheet-like morphology that is much thinner than the decagonal $BiVO_4$-**a** (Figure 4b). The $BiVO_4$-**h** sample (Figure 4c), synthesized at pH 4, exhibited a polyhedral shape with the size of about 1 μm. The $BiVO_4$-**i** sample (Figure 4d), synthesized at pH 7, produced rodlike products with a small particle size. The $BiVO_4$-**k** sample (Figure 4e), synthesized at pH 9, showed a trunk shape with small branches. At the highest pH value, 11, large agglomerates of trunks in the $BiVO_4$-**l** sample (Figure 4f) began to appear with the length of far more than 2 μm.

Identification of the (040) facet: Figure 5 shows the SEM and HRTEM images of $BiVO_4$-**a** and $BiVO_4$-**d** and show significant differences in morphology between the samples. To further demonstrate the morphology and identify the (040) facet, the HRTEM image of $BiVO_4$-**a** with the regular decagonal shape is given in Figure 5c. The SEM images of $BiVO_4$-**d** (Figure 5b) show sheet-like morphology with the average thickness of about 260 nm. The corresponding selected area electron diffraction (SAED) pattern in Figure 5d taken from the sheet-like $BiVO_4$-**d** sample reveals the growth orientation in accordance with the results of XRD measurements. As determined by XRD analysis, and with different *b* axis orientations for different sheets, the *d*-spacings measured from SAED (zone axis [010]) are 2.61 and 2.56 Å , which well agree with the lattice spacings of (200) and (002) monoclinic $BiVO_4$. The growth direction is along the (040) facet. Therefore, the sheet-like $BiVO_4$-**d** grows along the *b* axis as seen in the HRTEM images (Figure 4d). Figure 5e and f schematically illustrate the decagonal shape and sheet-like morphologies of $BiVO_4$ synthesized without and with a directing agent, respectively. The growth orientation of $BiVO_4$ prepared with the directing agent is along the (040) facet and the acidic medium also favors this facet.

Optical properties of $BiVO_4$ samples: Figure 6a shows the UV/Vis diffuse reflectance spectra of $BiVO_4$ samples synthesized with different amounts of directing agents. All samples showed absorption bands in the visible-light region. However, compared to the bare $BiVO_4$-**a**, no significant shifts of the absorption edges were observed for the samples synthesized by the addition of $TiCl_3$. The absorption onset edge was estimated to be at approximately 535 nm, corresponding

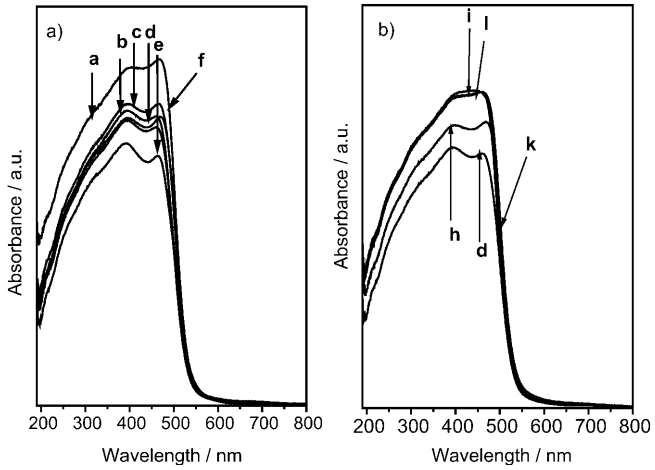

Figure 6. UV/Vis diffuse reflectance spectra of a) $BiVO_4$ synthesized with different concentrations of directing agent, $BiVO_4$-**a**–**f** and b) $BiVO_4$ synthesized with the optimum amount of directing agent under different pH values: $BiVO_4$-**d**, **h**, **i**, **k** and **l**.

to a bandgap of 2.31 eV, which is the characteristic absorption of monoclinic scheelite $BiVO_4$.[17,25] Figure 6b shows the UV/Vis diffuse reflectance spectra of $BiVO_4$ samples synthesized with the optimum amount of directing agent under different pH values. Similarly, almost no shifts in the absorption edge among the samples were observed. The absorption onset edges of $BiVO_4$ samples synthesized at various pH values were also estimated to be at approximately 535 nm. There are no clear differences in the absorption edge for all the synthesized $BiVO_4$ samples.

Raman spectra of $BiVO_4$ samples: Figure 7a shows Raman spectra of $BiVO_4$ synthesized with different concentrations of the directing agent. The Raman bands at around 210, 324, 366, 710, and 826 cm^{-1} were observed for all the samples, which are typical vibrational bands of monoclinic $BiVO_4$.[26–29] The Raman spectra of the samples synthesized with the optimum amount of the directing agent under different pH values, together with $BiVO_4$-**a**, are shown in Figure 7b. Again the typical vibrational bands of monoclinic $BiVO_4$ were observed for all samples.

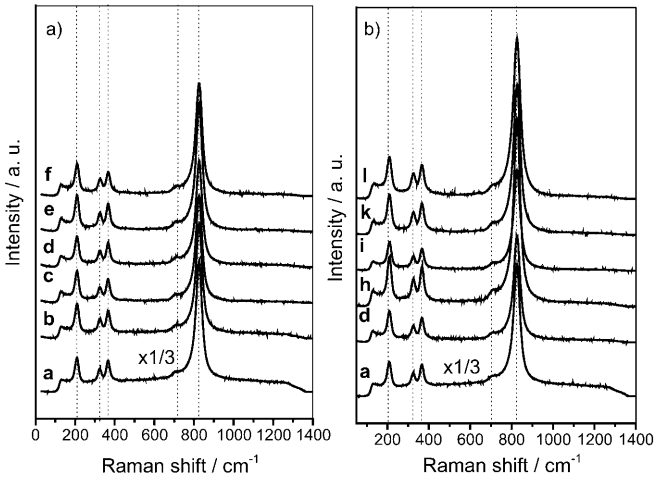

Figure 7. Raman spectra of a) $BiVO_4$ synthesized with different concentrations of directing agent by molar ratios of $BiVO_4$-**a**–**f** and b) $BiVO_4$-**a** and the $BiVO_4$ samples synthesized with the optimum amount of directing agent under different pH values: $BiVO_4$-**d**, **h**, **i**, **k** and **l**.

Relationship between the exposure of the (040) crystal facet and the activity of photocatalytic O_2 evolution: Figure 8 shows the variation of the photocatalytic rate of oxygen evolution for various $BiVO_4$ catalysts with different intensity ratios of (040)/(110) diffraction peaks as seen from XRD measurements. The rate of O_2 evolution 190 μmol h^{-1} for $BiVO_4$-**a** corresponds to the intensity ratio of the (040)/(110) at 1.1, and the highest rate of O_2 evolution is 310 μmol h^{-1} for the $BiVO_4$-**d** with the intensity ratio of (040)/(110) at 11.2. Figure 8 clearly shows that the photocatalytic activity of the $BiVO_4$ samples is enhanced with the increase of the (040)/(110) intensity ratio, indicating that the (040) facet plays a vital role in the photocatalytic oxidation of water.

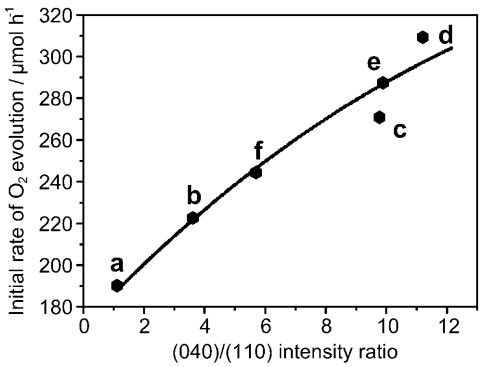

Figure 8. The correlations of the oxygen evolution rate with the (040)/(110) intensity ratio in the XRD patterns of the corresponding samples $BiVO_4$-**a**–**f**. Reaction conditions: catalyst, 0.3 g; light source, 300 W Xe lamp with cutoff filter ($\lambda \geq 420$ nm); $AgNO_3$ solution, 0.05 M, 200 mL.

Figure 9 shows the dependence of the initial rates of oxygen evolution on the (040)/(110) intensity ratio over $BiVO_4$ synthesized with the addition of optimum amount of directing agent at various hydrothermal pH values. Again the highest rate of O_2 evolution is that for $BiVO_4$-**d** (310 μmol h^{-1}), and the lowest rate of O_2 evolution is 25 μmol h^{-1} for the $BiVO_4$-**l**, with an intensity ratio at 0.6 of the (040)/(110) diffraction peaks; it can be seen that the activity increases with the increase of the (040)/(110) intensity ratio. Hence, the enhancement of photocatalytic O_2 evolution over the $BiVO_4$ sample with more (040) facet exposed has been observed can be correlated with the increase of the intensity of the (040) peak along the (040) facet, leading us to draw the conclusion that the (040) facet is a more active surface plane for O_2 evolution from water oxidation on $BiVO_4$ photocatalyst.

To exclude the effect of the residual Ti on the photocatalytic activity of $BiVO_4$, the initial rates of O_2 evolution for

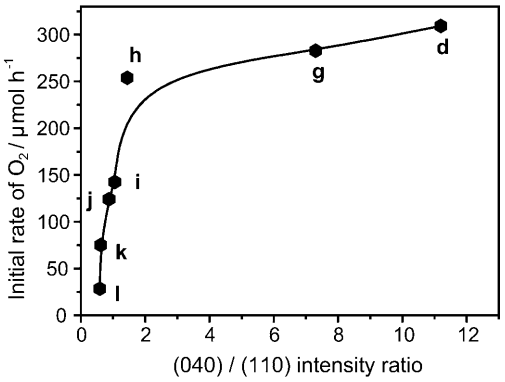

Figure 9. The dependence of the intensity ratio of the initial rates of oxygen evolution on the (040)/(110) intensity ratio over $BiVO_4$ synthesized with the addition of optimum amount of directing agent at various hydrothermal pH values of $BiVO_4$-**d**, **g**–**l**. The intensity ratio was observed using the (110) diffraction peak in the XRD pattern of $BiVO_4$ as the standard. Reaction conditions: catalyst, 0.3 g; light source, 300 W Xe lamp with cutoff filter ($\lambda \geq 420$ nm); $AgNO_3$ solution, 0.05 M, 200 mL.

$BiVO_4$-**a** and 1.2 at.% TiO_2-doped $BiVO_4$-**a** were given in Figure 10a. It can be seen that the photocatalytic activity of TiO_2/$BiVO_4$-**a** is almost the same as that of the pure $BiVO_4$-**a**; that is, the residual Ti has nearly no effect on the photocatalytic activity of O_2 evolution. Therefore, the residual Ti on the surface of $BiVO_4$ will play, at most, a very minor role in the increase of the rate of O_2 evolution for $BiVO_4$ samples. In addition, the doping effect of Ti was checked with $BiVO_4$ samples using other Ti-containing precursors as a directing agent. As also shown in Figure 10b, the $BiVO_4$ sample synthesized $[Ti\{OCH(CH_3)_2\}_4]$, $[Ti(OBu)_4]$, and $Ti(SO_4)_2$ showed much lower photocatalytic activities for O_2 evolution compared to the samples prepared with $TiCl_3$ as the directing agent. This demonstrates that the doping Ti only has no evident effect on the enhancement of the photocatalytic activity.

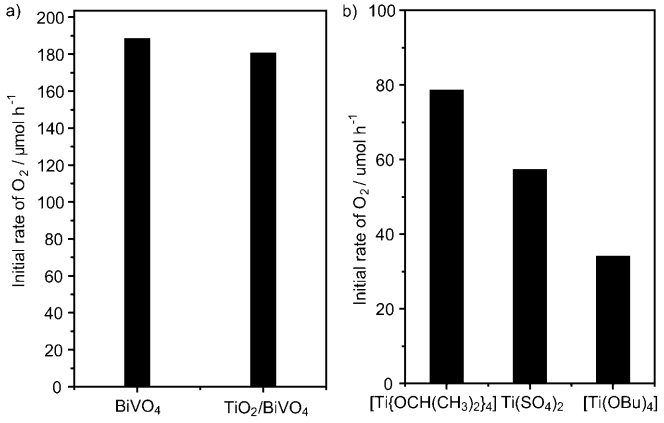

Figure 10. The initial rate of O_2 evolution over a) $BiVO_4$-**a** and $BiVO_4$-**a** doped with TiO_2 by impregnated method photocatalysts and b) $BiVO_4$ samples synthesized with Ti-containing precursors as directing agent from an aqueous silver nitrate solution under visible-light irradiation ($\lambda \geq 420$ nm). Reaction conditions: catalyst, 0.3 g; light source, 300 W Xe lamp with cutoff filter; $AgNO_3$ solution, 0.05 M, 200 mL.

Effects of the physical properties on the photocatalytic activity: Figure 11 shows the plots of the rate of photocatalytic O_2 evolution and surface area of $BiVO_4$ samples. The data

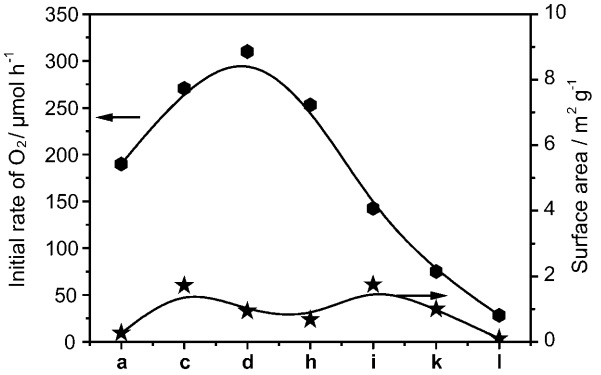

Figure 11. The rate of O_2 evolution and surface area of $BiVO_4$ samples synthesized by adding different amounts of $TiCl_3$ as directing agent and adding optimum amount of $TiCl_3$ under different pH values. Reaction conditions: catalyst, 0.3 g; light source, 300 W Xe lamp with cutoff filter; $AgNO_3$ solution, 0.05 M, 200 mL.

clearly indicate no apparent dependence of photocatalytic activity on surface area, as it can be seen that the $BiVO_4$-**i**, which has the largest surface area, showed lower activity compared with a sample with a relatively small surface area. As mentioned above, the relative intensity of the (040) peak in the XRD patterns of $BiVO_4$ corresponds to the exposure extent of the (040) facet. The change of the hydrophilicity upon the exposure of the (040) facet, which might also affect the photocatalytic activity, was also studied. The contact angles between sessile water droplets and the $BiVO_4$ flakes were almost same (see Supporting Information Figure S2), indicating that the hydrophilicity of the $BiVO_4$ samples is close to each other. After checking the correlations between physical properties (e.g., surface area and hydrophilicity) and photocatalytic activities, It turns out to be that the physical properties have a minor influence on the photocatalytic activity for $BiVO_4$ photocatalyst. It seems that the crystal facet plays a decisive role in the enhancement of photocatalytic activity.

The surface atomic configurations of the crystal facets in monoclinic $BiVO_4$: To understand how the (040) facet works on the atomic scale, the vertical view of the surface atomic configurations for the (040) facet in monoclinic $BiVO_4$ is shown in Figure 12a. The vertical view of the primitive cell for the (040) facet in the monoclinic $BiVO_4$ after geometry optimization is presented in Figure 12b. It is worth noting that the (040) facet provides the four-square multi-atomic center BiV_4 with Bi located at the center of square. Figure 12c and d show that the primitive cells of the (011) and (110) facets are composed of Bi_4V_2. The (040) facet is the

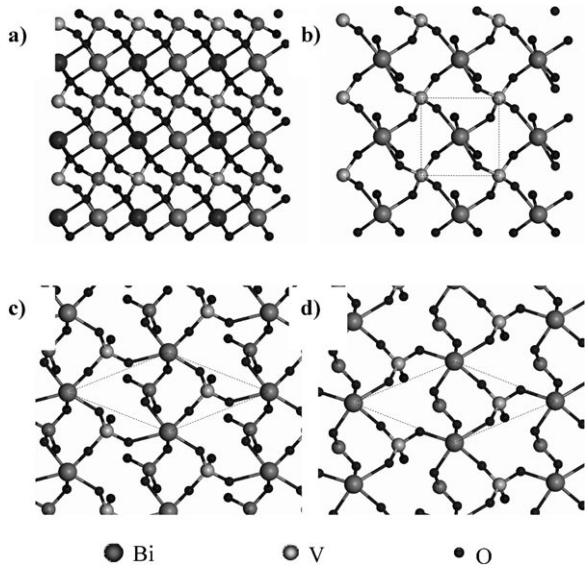

Figure 12. a) Vertical view of the surface atomic configurations for the (040) facet in monoclinic $BiVO_4$. The slab system of b) the (040) facet, c) the (110) facet and d) the (011) facet in the monoclinic $BiVO_4$ primitive cell after geometry optimization.

particular facet that possesses the BiV_4 multi-atomic center; this center seems to be analogous to the oxygen-evolving complex $CaMn_4$ in the photosynthesis system (PS II).[30–32] Current structural models of the oxygen-evolving complex show that the oxos within the $CaMn_4$ cluster are singly bonded to two and three Mn centers of the core, and in the dangler model,[33] an oxos is proposed to be multiply bonded to the dangling bond of Mn, which is directly responsible for the four-electron transfer for the O_2 evolution.[34,35] Both BiV_4 and $CaMn_4$ can provide oxo-bridges and multi-coordinate oxygen atoms, which may be a common structure for the O_2 evolution during the photocatalytic water oxidation. It is proposed that the $BiVO_4$ with more exposed (040) facet provides more multi-atomic centers BiV_4, which may be more facile for the multi-electron transfer involved in the O_2 evolution. To obtain a deeper understanding of the enhanced water oxidation activity on the (040) facet, more detailed experiments and theoretical calculations are underway.

Conclusion

The monoclinic $BiVO_4$ with a highly exposed (040) facet can be synthesized by adjusting the amount of the directing agent and the pH values for a hydrothermal synthesis. The photocatalytic water oxidation activity of $BiVO_4$ correlates very well with the extent of exposure of the (040) facet. The (040) facet is assumed to provide a multi-atomic BiV_4 centre, which may be the origin of the active sites for photocatalytic O_2 evolution. Our findings show that the controllable growth along with a more active crystal facet of the photocatalyst is an efficient strategy for enhancing the photocatalytic activity.

Experimental Section

Catalyst preparation: $BiVO_4$ samples with different growth extent of the (040) facet were synthesized by the addition of an appropriate amount of $TiCl_3$ (directing agent) in aqueous solution (0–100 μL) to a solution of NH_4VO_3 (6.0 mM) and $Bi(NO_3)_3{\cdot}5H_2O$ (6.0 mM) in nitric acid (30 mL; 2 M) at room temperature. The pH value of the reaction mixture was adjusted to 2 with ammonia solution (25–28 wt.%) under vigorous stirring. After stirring for 0.5 h at room temperature, the reaction mixture was transferred into a Teflon-lined stainless steel autoclave, and aged at 473 K for 24 h. Filtration and washing with plenty amount of water afforded vivid yellow powder, which was dried at 353 K and then calcined at 673 K for 2 h. In order to find out the optimum amount of $TiCl_3$ loading, a series of $BiVO_4$ samples with the Ti/Bi ratio ranging from 0 to 2.0 at.% were synthesized and denoted as $BiVO_4$-**a**, **b**, **c**, **d**, **e**, **f** as shown in Table S1 in the Supporting Information. The effect of pH values was also studied by varying the pH value from 2.5 to 11during synthesis, and the samples synthesized at pH of 2.5, 4, 7.5, 8, 9, 11are denoted as **g**, **h**, **i**, **j**, **k**, **l**, respectively (Table S1 in the Supporting Information).

Catalyst characterization: The synthesized samples were characterized by X-ray powder diffraction (XRD) on a Rigaku D/Max-2500/PC powder diffractometer. Each sample powder was scanned using $Cu_{K\alpha}$ radiation with an operating voltage of 40 kV and an operating current of 200 mA. The scan rate of $5°\,min^{-1}$ was applied to record the XRD patterns in the range of 8–80° at a step size of 0.02°. UV/Vis diffuse reflectance spectra were recorded on a UV/Vis spectrophotometer (JASCO V-550) equipped with an integrating sphere. The morphologies and particle sizes were examined by scanning electron microscopy (SEM) taken with a Quanta 200 FEG scanning electron microscope. HRTEM micrographs were taken on a JEM-2000eX transmission electron microscope. The surface areas of the samples were taken with a Micromeritics ASAP 2000 adsorption analyzer. Raman scattering spectra were recorded in back-scattering geometry on an Acton Raman spectrometer equipped with a liquid nitrogen-cooled CCD detector at a resolution of $4\,cm^{-1}$. A 532 nm semiconductor laser was used as the excitation source with the power of 60 mW. The contact angles formed between sessile water droplets and the flakes were measured using a contact angle measuring system JC 2000 A.

Photocatalytic reactions: All experiments were performed with a quartz tube at room temperature. The photocatalytic O_2 evolution reactions were carried out in a closed gas circulation and evacuation system using a 300 W Xe lamp (Ushio-CERMAX LX300) and optical cut-off filter (Kenko, L-42; $\lambda > 420$ nm). The photocatalyst (0.3 g) was dispersed in an aqueous $AgNO_3$ solution (0.05 M, 200 mL) in a Pyrex reaction cell and thoroughly degassed by evacuation in order to drive off the air inside. The amount of evolved O_2 was determined by an on-line gas chromatograph (Shimadzu GC-8 A, TCD, Ar carrier). The maximum rates of O_2 evolution (denoted as O_2 evolution rate, hereafter) for the first hour (before deactivation of the catalyst) were used for evaluating the photocatalytic activity of the samples.

Acknowledgements

This work was financially supported by the National Natural Science Foundation of China (Grant No. 20503034, 20673112), Programme Strategic Scientific Alliances between China and the Netherlands (Grant No. 2008DFB50130). The authors thank Prof. H. X. Han and Prof. Dr. W. X. Li of State Key Laboratory of Catalysis, Dalian Institute of Chemical Physics, Chinese Academy of Sciences, for revising the paper and the helpful discussion, respectively.

[1] K. Takanabe, T. Uzawa, X. C. Wang, K. Maeda, M. Katayama, J. Kubota, A. Kudo, K. Domen, *Dalton Trans.* **2009**, 10055–10062.
[2] X. D. Tang, H. Q. Ye, Z. Zhao, H. Liu, C. X. Ma, *Catal. Lett.* **2009**, *133*, 362–369.
[3] K. Maeda, K. Domen, *Chem. Mater.* **2010**, *22*, 612–623.
[4] A. Mills, S.-K. Lee, *Platinum Met. Rev.* **2003**, *47*, 2–12.
[5] A. Kudo, Y. Miseki, *Chem. Soc. Rev.* **2009**, *38*, 253–278.
[6] F. Seker, K. Meeker, T. F. Kuech, A. B. Ellis, *Chem. Rev.* **2000**, *100*, 2505–2536.
[7] G. A. Somorjai, *Introduction to Surface Chemistry and Catalysis*, Wiley, New York **1994**, pp. 461–467.
[8] H. G. Yang, C. H. Sun, S. Z. Qiao, J. Zou, G. Liu, S. C. Smith, H. M. Cheng, G. Q. Lu, *Nature* **2008**, *453*, 638–642.
[9] G. Liu, C. H. Sun, H. G. Yang, S. C. Smith, L. Z. Wang, G. Q. Lu, H. M. Cheng, *Chem. Commun.* **2010**, *46*, 755–757.
[10] X. Han, Q. Kuang, M. Jin, Z. Xie, L. Zheng, *J. Am. Chem. Soc.* **2009**, *131*, 3152–3153.
[11] D. Q. Zhang, G. S. Li, X. F. Yang, J. C. Yu, *Chem. Commun.* **2009**, 4381–4383.
[12] J. H. Zeng, B. B. Jin, Y. F. Wang, *Chem. Phys. Lett.* **2009**, *472*, 90–95.
[13] A. McLaren, T. Valdes-Solis, G. Q. Li, S. C. Tsang, *J. Am. Chem. Soc.* **2009**, *131*, 12540–12541.
[14] L. Zhang, D. R. Chen, X. L. Jiao, *J. Phys. Chem. B* **2006**, *110*, 2668–2673.
[15] G. C. Xi, J. H. Ye, *Chem. Commun.* **2010**, *46*, 1893–1895.
[16] A. Kudo, K. Omori, H. Kato, *J. Am. Chem. Soc.* **1999**, *121*, 11459–11467.
[17] A. Kudo, K. Ueda, H. Kato, I. Mikami, *Catal. Lett.* **1998**, *53*, 229–230.
[18] J. Q. Yu, A. Kudo, *Adv. Funct. Mater.* **2006**, *16*, 2163–2169.
[19] K. Sayama, A. Nomura, T. Arai, T. Sugita, R. Abe, M. Yanagida, T. Oi, Y. Iwasaki, Y. Abe, H. Sugihara, *J. Phys. Chem. B* **2006**, *110*, 11352–11360.
[20] H. Kato, Y. Sasaki, A. Wase, A. Kudo, *Bull. Chem. Soc. Jpn.* **2007**, *80*, 2457–2464.
[21] H. Kato, M. Hori, R. Konta, Y. Shimodaira, A. Kudo, *Chem. Lett.* **2004**, *33*, 1348–1349.
[22] Y. Sasaki, H. Nemoto, K. Saito, A. Kudo, *J. Phys. Chem. C* **2009**, *113*, 17536–17542.
[23] W. Z. Yin, W. Z. Wang, L. Zhou, S. M. Sun, L. Zhang, *J. Hazard. Mater.* **2010**, *173*, 194–199.
[24] Y. N. Guo, X. Yang, F. Y. Ma, K. X. Li, L. Xu, X. Yuan, Y. H. Guo, *Appl. Surf. Sci.* **2010**, *256*, 2215–2222.
[25] A. Kudo, K. Omori, H. Kato, *J. Am. Chem. Soc.* **1999**, *121*, 11459–11467.
[26] A. W. Sleight, H. y. Chen, A. Ferretti, D. E. Cox, *Mater. Res. Bull.* **1979**, *14*, 1571–1581.
[27] J. B. Liu, H. Wang, S. Wang, H. Yan, *Mater. Sci. Eng. B* **2003**, *104*, 36–39.
[28] A. Galembeck, O. L. Alves, *Thin Solid Films* **2000**, *365*, 90–93.
[29] J. Q. Yu, A. Kudo, *Chem. Lett.* **2005**, *34*, 850–851.
[30] K. N. Ferreira, T. M. Iverson, K. Maghlaoui, J. Barber, S. Iwata, *Science* **2004**, *303*, 1831–1838.
[31] M. Haumann, P. Liebisch, C. Muller, M. Barra, M. Grabolle, H. Dau, *Science* **2005**, *310*, 1019–1021.
[32] J. Yano, J. Kern, K. Sauer, M. J. Latimer, Y. Pushkar, J. Biesiadka, B. Loll, W. Saenger, J. Messinger, A. Zouni, V. K. Yachandra, *Science* **2006**, *314*, 821–825.
[33] J. M. Peloquin, R. D. Britt, *Biochim. Biophys. Acta-Bioenerg.* **2001**, *1503*, 96–111.
[34] G. W. Brudvig, *Philos. Trans. R. Soc. Lond. B Biol. Sci.* **2008**, *363*, 1211–1218.
[35] J. Yano, V. K. Yachandra, *Inorg. Chem.* **2008**, *47*, 1711–1726.

Received: June 10, 2010
Published online: November 29, 2010

